

Multi-Objective Optimization for Quantum Rectangular Cycle with Power, Efficiency and Efficient Power

X. XIE^a, L. CHEN^{b,c,d,*}, Y. YIN^{a,b} AND S. SHI^{b,c,d}

^a*School of Optical Information and Energy Engineering, Wuhan Institute of Technology, Wuhan 430205, China*

^b*Institute of Thermal Science and Power Engineering, Wuhan Institute of Technology, Wuhan 430205, China*

^c*Hubei Provincial Engineering Technology Research Center of Green Chemical Equipment, Wuhan 430205, China*

^d*School of Mechanical & Electrical Engineering, Wuhan Institute of Technology, Wuhan 430205, China*

Received: 01.05.2023 & Accepted: 11.12.2023

Doi: [10.12693/APhysPolA.145.16](https://doi.org/10.12693/APhysPolA.145.16)

*e-mail: lingenchen@hotmail.com

This paper establishes a quantum rectangular heat engine model by applying finite-time thermodynamics. The working medium is countless particles trapped in a one-dimensional infinite potential well. Taking into account heat leakage between the system and the outside, expressions for thermal efficiency (η), dimensionless power (\bar{P}), and dimensionless efficient power (\bar{W}_{ep}) of quantum rectangular heat engine are derived, and its optimal performance is studied. System performance \bar{P} , η , and \bar{W}_{ep} are optimized firstly by taking the width ratio of the potential well as the optimization variable. The outcomes show that the relationship curve between \bar{P} and η is a loop-shaped curve. With an increase in heat leakage coefficient, the optimal design range of the quantum rectangular heat engine becomes smaller. The relationship curve between the efficient power and width ratio of the potential well is parabolic-like. The relationship curve between \bar{W}_{ep} and η is a loop-shaped curve. The efficiency of the quantum rectangular heat engine at $\bar{W}_{ep\max}$ operating point is greater than that at P_{\max} operating point. Secondly, multi-objective optimization is applied with η , \bar{P} , and \bar{W}_{ep} as optimization objectives by applying NSGA-II, and the optimal design scheme is achieved by applying TOPSIS, LINMAP, and Shannon entropy decision-making approaches. The smallest deviation index inferred by the Shannon entropy approach is 0.0269. The design scheme is closest to the ideal scheme.

topics: finite-time thermodynamics; quantum rectangular heat engine (QRHE); power, multi-objective optimization, thermal efficiency and efficient power

1. Introduction

In the wake of the advancement of micro-nano and low-temperature technology, the quantum characteristics of the thermodynamic cycle should be considered when analyzing and optimizing the quantum thermodynamic cycle [1–6]. Since Scovil and Schulz–DuBois [7] first proposed a three-level quantum heat engine model in 1959, many scholars have proposed quantum energy conversion devices and quantum thermodynamic cycles using various quantum systems as working fluids, such as particles in one-dimensional infinite potential well (OIPW) [8], relativistic particles in OIPW [9], spin system [10], resonance subsystem [11], quantum gas [12], etc. Using these common quantum working media (WM) and applying finite-time thermodynamics (FTT) [13–27], many scholars have studied

the thermodynamic properties of quantum Stirling cycle [8], Carnot cycle [10, 11, 28], Diesel cycle [29], Brayton cycle [30, 31], Otto cycle [32, 33], etc. and got numerous meaningful results.

Among the optimized performance parameters of heat engines, power and efficiency have been widely studied as the two most important performance parameters [34–37]. In addition, efficient power (product of efficiency and power) is also one of the important performance indicators, which was first proposed by Yan [38] and named by Yilmaz [39]. Subsequently, many scholars have optimized the performance of various macro and quantum thermal cycles with efficient power as the optimization objective [40–42]. By using this objective, Quan et al. [40] investigated the properties of a quantum Carnot heat engine. Singh [41] studied the properties of a three-level quantum heat engine.

Kaur et al. [42] optimized the performance of an endoreversible quantum dot heat engine. At present, much research shows that the efficiency and power of the forward-cycle can be achieved with larger values at the maximum efficient power point.

A new forward-cycle model is the rectangular cycle, which has two isochoric processes and two isobaric processes. It is so named because it is shown as a rectangle on the pressure–volume chart. Da Silva Ferreira [43] was the first to obtain the output power and efficiency formula of the rectangular cycle by applying classical thermodynamic theory. On this basis, Liu et al. [44] applied the theory of FTT to study power and efficiency characteristics with an air standard endoreversible rectangular cycle model with heat transfer losses. The performance of the irreversible rectangular cycle considering heat transfer losses and friction factor was also analyzed by Liu et al. [44]. Wang et al. [45, 46] investigated the influence of the specific-heat model of WM on the performance of endoreversible and irreversible rectangular cycles. Articles [43–46] all concern macroscopic rectangular cycle as the study object without considering the quantum properties of the working medium.

A thermal cycle often has multiple objective functions. If a single objective is used to optimize the system, it is often impossible to balance the relationship between the different objective functions, and thus the cycle performance cannot be optimized. In an effort to weigh the merits and demerits of each performance index, many researchers presented the idea of multi-objective optimization (MOO) [44–47]. Ahmadi et al. [47] investigated the efficiency, power, and pressure loss features of the Stirling heat engine cycle and applied the NSGA algorithm to carry out triple-objective optimization. Gong et al. [48] and Liu et al. [49] studied power density and efficient power features of the endoreversible macro rectangular cycle and applied the NSGA-II algorithm to further realize the four-objective optimization of the macro irreversible rectangular cycle. Qiu et al. [50, 51] investigated the efficient power characteristics of simple endoreversible and irreversible closed Brayton cycles and applied the NSGA-II algorithm to optimize five objectives: cycle thermal efficiency, power, power density, ecological function, and efficient power. NSGA-II algorithm has also been applied to MOOs for other macro thermal cycles and processes, such as Dual [52], Stirling [53], porous medium cycle [54], organic Rankine cycle [55], chemical pump [56], Otto cycle [57], and membrane reactors [58, 59].

In the field of quantum thermodynamics, Erdman et al. [60] used reinforcement learning to identify the Pareto frontier of quantum dot heat engine driven by quantum fluctuations, and the optimization results took into account both power and efficiency.

On the basis of [44–46, 48, 49], this paper will first introduce FTT theory to the quantum rectangular heat engine (QRHE) cycle with WM of

countless particles trapped in OIPW. The QRHE cycle consists of four processes: (i) equal potential well width heat absorption process, (ii) equal potential well force heat absorption process, (iii) equal potential well width heat release process, and (iv) equal potential well force heat release process. Assuming that the wall of the potential well moves with a constant velocity and considering heat leakage loss between the heat source and sink, expressions for thermal efficiency (η), dimensionless power (\bar{P}), and dimensionless efficient power (\bar{W}_{ep}) of the QRHE cycle will be derived, and its optimal performance will be studied. System performances \bar{P} , η , and \bar{W}_{ep} will be optimized firstly by taking the width ratio of potential well as the optimization variable. Secondly, MOO will be applied with \bar{P} , η , and \bar{W}_{ep} as optimization objectives, and the optimal design scheme will be achieved by applying TOPSIS, LINMAP, and Shannon entropy approaches.

2. Quantum-mechanical description of the system

According to [61], considering the particle trapped in OIPW, its wave function satisfies

$$\frac{d^2\phi(x)}{dx^2} + \frac{2mE}{\hbar^2}\psi(x) = 0, \quad (1)$$

where $\psi(x)$ is the wave function required to satisfy boundary conditions $\psi(0) = 0$ and $\psi(L) = 0$, m is the mass of a particle, \hbar is the scaled Planck constant, and E is the energy eigenvalue of particle. The wave function may be given by

$$\psi(x) = \sum_{n=1}^{\infty} a_n \sqrt{\frac{2}{L}} \sin\left(\frac{n\pi}{L}x\right) \quad (n = 1, 2, \dots). \quad (2)$$

The coefficient a_n satisfies the normalization condition

$$\sum_{n=1}^{\infty} |a_n|^2 = \sum_{n=1}^{\infty} p_n = 1, \quad (3)$$

where $p_n = |a_n|^2$ is the probability of particles appearing at the n -th energy level. According to [61], the energy eigenvalue of the particle is expressed as follows

$$E_n = \frac{\pi^2 \hbar^2}{2mL^2} n^2 \quad (n = 1, 2, \dots), \quad (4)$$

where n is a quantum number. Therefore, the expected value of the Hamiltonian of the system is

$$E(L) = \sum_{n=1}^{\infty} |a_n|^2 E_n = \sum_{n=1}^{\infty} p_n E_n. \quad (5)$$

In the macro thermodynamic cycle, the system can work externally through the reciprocating motion of the piston. In the quantum cycle, according to [62, 63], it can be assumed that the potential well wall of OIPW reciprocates, thus realizing the external work of the system. The energy eigenvalue and wave function of the system are functions of the width (L) of the potential well. With the

change in width (L), they change. Therefore, the generalized force applied to the wall of a potential well is

$$Y_n = -\frac{dW}{dy_n}, \quad (6)$$

where dy_n stands for generalized displacement corresponding to generalized force Y_n . Differentiating (5) yields

$$dE(L) = \sum_{n=1}^{\infty} (p_n dE_n + E_n dp_n), \quad (7)$$

$$dE(L) = dQ - F dL. \quad (8)$$

From (4)–(8), one can find that the force applied to the wall of the potential well is

$$F = -\frac{dE}{dL} = \sum_{n=1}^{\infty} p_n \frac{\pi^2 \hbar^2}{mL^3} n^2. \quad (9)$$

3. QRHE cycle

In this paper, the particles in OIPW are taken as WM. The cycling WM is composed of countless identical particles. According to [64, 65], only the first excited and ground states are considered. In a multi-stage system, the occupancy probability of the n -th excited state is $p_n = \exp(-E_n/(k_B T)) / \sum_n \exp(-E_n/(k_B T))$. It can be concluded that the occupancy probability p_n decreases with the increase in E_n and the decrease in T . At an extremely low-temperature environment, the occupancy probability in the n -th ($n > 2$) excited state can be ignored, and only the lowest two energy levels can be considered. Of course, a two-stage system is simpler than a multi-stage system. On the other hand, two-stage systems can often be seen in quantum energy conversion systems. Therefore, only the first excited and ground states are considered. The probabilities of particles at each energy level are described by the Gibbs distribution. Figures 1 and 2 are, respectively, the F – L diagram and T – s diagram of the QRHE model.

The QRHE cycle consists of two equal potential well force processes and two equal potential well width processes, which correspond to the isobaric process and isochoric process in the macro thermodynamic cycle, respectively. The cycle is an irreversible quantum cycle with a heat leakage loss between the source and the sink.

Thin layers grown alternately by two different semiconductor materials will form a multi-layer structure. According to [66], if the width of the thin layer reaches the quantum scale, this multi-layer structure can be called a quantum well. Because it is limited by quantum scale (comparable to the de Broglie wavelength of particles) in one direction and macroscopic scale in the other two directions, the energy level of particles in the thin layer can be described by OIPW. According to [67], the common method of fabricating quantum

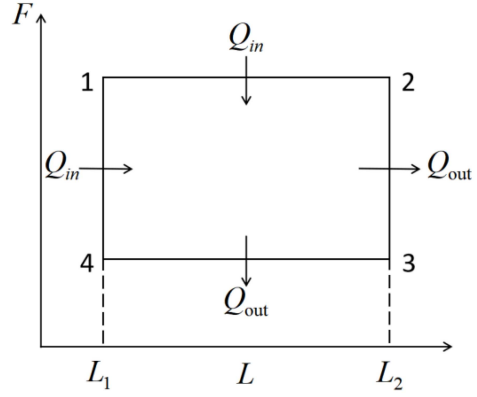


Fig. 1. F – L diagram of QRHE cycle.

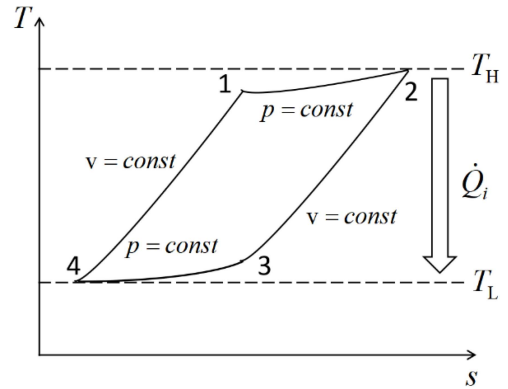


Fig. 2. T – s diagram of QRHE cycle.

wells is to place a narrow-bandgap semiconductor, e.g., typical InGaAs/GaAs quantum wells, between two wide-bandgap semiconducting materials. Holes, electrons, or excitons in quantum wells can form discrete energy levels on the basis of the quantum effect. According to [68, 69], with the realization of various quantum heat engine cycles in experiments, it is believed that in the near future, quantum rectangular cycles can also be realized in the laboratory.

Process $1 \rightarrow 2$ involves placing force sensors at both ends of the multi-layer structure. As the system absorbs heat from a high-temperature source, external voltage $U(t)$ is used to adjust the width of the thin layer to keep the reading of the force sensor unchanged. In the $2 \rightarrow 3$ process, the external voltage $U(t)$ is kept constant. The particles in the trap experience a process of equal potential well width. Processes $3 \rightarrow 4$ and $4 \rightarrow 1$ are similar to processes $1 \rightarrow 2$ and $2 \rightarrow 3$. Since both the source and sink interact with trapped particles through a multi-layer structure, there exists heat leakage (Q_e) between source and sink. This article mainly studies the effect of the potential well width ratio on the performance of quantum rectangular cycles. The width ratio of the potential well can be determined by the width ratio of the initial and final state of the process when both ends of the sample are free ends.

3.1. Equal potential well force endothermic process

Process 1 \rightarrow 2 is an endothermic process with equal potential well force. The force acting on the potential well wall does not vary during this process, which is similar to the isobaric process in the macro cycle. Therefore, one has

$$dQ = dE + F_{\text{const}} dL. \quad (10)$$

When the system is in state point 1, the force applied to the potential well wall is

$$F_1 = p_{11}F_{11} + p_{12}F_{12} = \frac{\pi^2 \hbar^2}{mL_1^3}(1 + 3p_{12}), \quad (11)$$

where p_{ik} is the occupancy probability of particles ($i = 1, 2, 3, 4$ represents the state point; $k = 1$ represents the ground state, and $k = 2$ represents the first excited state); F_{ik} is the force exerted by the particles on the wall of the potential well ($i = 1, 2, 3, 4$ represents the state point; $k = 1$ represents the ground state, and $k = 2$ represents the first excited state). When the system is in state point 2, the force applied to the potential well wall is

$$F_2 = p_{21}F_{21} + p_{22}F_{22} = \frac{\pi^2 \hbar^2}{mL_2^3}(1 + 3p_{22}). \quad (12)$$

Force on the wall of the potential well is constant from the state point 1 to the state point 2. From (11) and (12), one has

$$\frac{1}{L_1^3}(1 + 3p_{12}) = \frac{1}{L_2^3}(1 + 3p_{22}). \quad (13)$$

Because this process is an equipotential well force process, one has

$$F_1 = F_{1-2} = F_2, \quad (14)$$

where $F_{i-i'}$ is the force exerted by the particles on the wall of the potential well during the cycle ($i = 1, 2, 3, 4$ represents the state point, $i' = 1, 2, 3, 4$ represents the state point). Therefore, the external work of the system in process 1 \rightarrow 2 is

$$W_{12} = \int_{L_1}^{L_2} dL F_{1-2} = \frac{\pi^2 \hbar^2}{mL_1^3}(1 + 3p_{12})(L_2 - L_1). \quad (15)$$

At state point 1, the total energy is

$$E_1 = p_{11}E_{11} + p_{12}E_{12} = \frac{\pi^2 \hbar^2}{2mL_1^2}(1 + 3p_{12}). \quad (16)$$

At state point 2, the total energy is

$$E_2 = p_{21}E_{21} + p_{22}E_{22} = \frac{\pi^2 \hbar^2}{2mL_2^2}(1 + 3p_{22}). \quad (17)$$

According to [8, 9], substituting (15)–(17) into (10) yields absorbed heat

$$\begin{aligned} Q_{12} = E_2 - E_1 + W_{12} = & \\ & \frac{\pi^2 \hbar^2}{2mL_1^2} \left[\left(\frac{L_1^2}{L_2^2} + \frac{3L_1^2}{L_2^2} p_{22} - 1 - 3p_{12} \right) \right. \\ & \left. + (1 + 3p_{12}) \left(\frac{L_2}{L_1} - 1 \right) \right]. \end{aligned} \quad (18)$$

3.2. Equal potential well width exothermic process

Process 2 \rightarrow 3 is an exothermic process with equal potential well width. The width of the wall of the potential well does not vary during this process. The system does not exchange work with the external environment, which is analogous to the fact that the volume remains unchanged under the isochoric process in the macro cycle. The first law of thermodynamics can be given as

$$dQ = dE. \quad (19)$$

At state point 3, the total energy is

$$E_3 = p_{31}E_{31} + p_{32}E_{32} = \frac{\pi^2 \hbar^2}{2mL_2^2}(1 + 3p_{32}). \quad (20)$$

Substituting (17)–(20) into (19) yields heat released by the system in this process

$$Q_{23} = E_3 - E_2 = \frac{3\pi^2 \hbar^2}{2mL_2^2}(p_{32} - p_{22}). \quad (21)$$

3.3. Equal potential well force exothermic process

Process 3 \rightarrow 4 is an exothermic process with equal potential well force. When the system is in state point 3, the force applied to the potential well wall is

$$F_3 = p_{31}F_{31} + p_{32}F_{32} = \frac{\pi^2 \hbar^2}{mL_2^3}(1 + 3p_{32}). \quad (22)$$

When the system is in state point 4, the force applied to the potential well wall is

$$F_4 = p_{41}F_{41} + p_{42}F_{42} = \frac{\pi^2 \hbar^2}{mL_1^3}(1 + 3p_{42}). \quad (23)$$

From state point 3 to state point 4, the force applied to the wall of the potential well is constant. From (11) and (12), one has

$$\frac{1}{L_2^3}(1 + 3p_{32}) = \frac{1}{L_1^3}(1 + 3p_{42}). \quad (24)$$

In an equipotential well force process, there is

$$F_3 = F_{3-4} = F_4. \quad (25)$$

Therefore, the external work of the system in process 3 \rightarrow 4 is

$$W_{34} = \int_{L_2}^{L_1} dL F_{3-4} = \frac{\pi^2 \hbar^2}{mL_1^3}(1 + 3p_{42})(L_1 - L_2). \quad (26)$$

At state point 4, total energy is

$$E_4 = p_{41}E_{41} + p_{42}E_{42} = \frac{\pi^2 \hbar^2}{2mL_1^2}(1 + 3p_{42}). \quad (27)$$

Substituting (20), (26), and (27) into (10) yields heat released in this process as follows

$$\begin{aligned} Q_{34} = E_4 - E_3 + W_{34} = & \\ & \frac{\pi^2 \hbar^2}{2mL_1^2} \left[\left(1 + 3p_{42} - \frac{L_1^2}{L_2^2} - \frac{3L_1^2}{L_2^2} p_{32} \right) \right. \\ & \left. + (1 + 3p_{42}) \left(1 - \frac{L_2}{L_1} \right) \right]. \end{aligned} \quad (28)$$

3.4. Equal potential well width endothermic process

Process 4 → 1 is an endothermic process with equal potential well width. Substituting (16) and (27) into (19) yields heat absorbed during this process

$$Q_{41} = E_1 - E_4 = \frac{3\pi^2\hbar^2}{2mL_1^3}(p_{12}-p_{42}). \quad (29)$$

4. Main performance parameters of QRHE cycle

In the actual process, there is heat leakage between the source and the sink. According to [8, 9, 61], it can be assumed that the heat leakage between high and low-temperature heat sources in each cycle is part of the ground state energy at the midpoint of the F - L plane. The heat leakage rate is defined by

$$\dot{Q}_i = \frac{\pi^2\hbar^2}{2mL_1^2}\alpha, \quad (30)$$

where α [s⁻¹] is a constant. Heat leakage amount per cycle is

$$Q_e = \dot{Q}_i\tau, \quad (31)$$

where τ is the cycle period. Therefore, it can be obtained from (18), (30), and (32) that heat absorbed from a high-temperature source can be described as

$$Q_H = Q_{41} + Q_{12} + Q_e = \frac{\pi^2\hbar^2}{2mL_1^2} \left[\left(\frac{L_1^2}{L_2^2} + \frac{3L_1^2}{L_2^2}p_{22} - 1 - 3p_{42} \right) + (1 + 3p_{12}) \left(\frac{L_2}{L_1} - 1 \right) + \alpha\tau \right]. \quad (32)$$

It can be obtained from (18), (30), and (32) that heat released to a low-temperature sink is

$$Q_L = Q_{23} + Q_{34} + Q_e = \frac{\pi^2\hbar^2}{2mL_1^2} \left[\left(1 + 3p_{42} - \frac{L_1^2}{L_2^2} - \frac{3L_1^2}{L_2^2}p_{22} \right) + (1 + 3p_{42}) \left(1 - \frac{L_2}{L_1} \right) + \alpha\tau \right]. \quad (33)$$

The relaxation time of the quantum system is in the order of \hbar/E . If the cycle period is slow ($\hbar/E \ll \tau$) relative to this time, these processes can be regarded as infinitely slow and can be regarded as quasi-static processes. It is assumed that the wall motion of OIPW is similar to the piston motion in the macro thermodynamic cycle, according to [67, 70]. The wall of the potential well is

assumed to move with velocity $v(t)$, and the average velocity is \bar{v} . One can obtain

$$L_2 - L_1 = \int_{L_1}^{L_2} dt v(t) = \bar{v}\tau_{12}. \quad (34)$$

In the cycle process 1 → 2 and process 3 → 4, the required time is

$$\tau_{12} = \tau_{34} = \frac{L_2 - L_1}{\bar{v}}. \quad (35)$$

The internal energy of the system changes during cycle process 2 → 3 and process 4 → 1. Similar to the macro thermodynamic process, the internal energy of the system in this process is a single-valued function of the temperature. The change rates of internal energy and temperature of the system as functions of time are assumed to be constants. Suppose that the change rate of system temperature with time is

$$\frac{dT}{dt} = \pm M_i, \quad (36)$$

where M is the average change rate of WM temperature with time in the process of equal potential well width. The negative sign indicates exothermic process 2 → 3 ($i = 1$), and the positive sign indicates endothermic process 4 → 1 ($i = 2$). Therefore, the time required for process 2 → 3 and process 4 → 1 can be obtained as

$$\tau_{23} = \frac{T_2 - T_3}{M_1}, \quad (37)$$

$$\tau_{41} = \frac{T_1 - T_4}{M_2}. \quad (38)$$

The cycle period can be obtained from (36), (38), and (39) as follows

$$\tau = \tau_{12} + \tau_{23} + \tau_{34} + \tau_{41} = \frac{2(L_2 - L_1)}{\bar{v}} + \frac{T_2 - T_3}{M_1} + \frac{T_1 - T_4}{M_2}. \quad (39)$$

The net work done by the system can be obtained from (15) and (26) as follows

$$W = \frac{3\pi^2\hbar^2}{mL_1^3}(p_{12}-p_{42})(L_2-L_1). \quad (40)$$

The power of the QRHE cycle can be expressed as

$$P = \frac{W}{\tau} = \frac{3\pi^2\hbar^2\bar{v}}{2mL_1^3}(x-1)(p_{12}-p_{42}) \times \left[(x-1) + \frac{\bar{v}T_4}{2L_1M_1} \left(\frac{T_2}{T_4} - \frac{T_3}{T_4} \right) + \frac{\bar{v}T_4(r-1)}{2L_1M_2} \right]^{-1}, \quad (41)$$

where $x = L_2/L_1$ ($x > 1$) is the potential well width ratio, and $r = T_1/T_4$ ($r > 1$) is the ratio of the temperature of WM.

The thermal efficiency of the QRHE cycle is

$$\eta = \frac{W}{Q_H} = \frac{6(x-1)(p_{12}-p_{42})}{\left(\frac{1}{x^2} + \frac{3}{x^2}p_{22} - 1 - 3p_{42} \right) + (1+3p_{12})(x-1) + \alpha \left[(x-1) + \frac{\bar{v}T_4}{2L_1M_1} \left(\frac{T_2}{T_4} - \frac{T_3}{T_4} \right) + \frac{\bar{v}T_4}{2L_1M_2} (r-1) \right]}. \quad (42)$$

Dimensionless power of QRHE cycle is defined as

$$\bar{P} = P/P_{\max}. \quad (43)$$

According to [38, 39], the efficient power of the QRHE cycle is defined as

$$W_{ep} = P\eta = \frac{6(x-1)^2(p_{12}-p_{42})^2 \left[(x-1) + \frac{\bar{v}T_4}{2L_1M_1} \left(\frac{T_2}{T_4} - \frac{T_3}{T_4} \right) + \frac{\bar{v}T_4}{2L_1M_2} (r-1) \right]^{-1}}{\left(\frac{1}{x^2} + \frac{3}{x^2}p_{22} - 1 - 3p_{42} \right) + (1+3p_{12})(x-1) + \alpha \left[(x-1) + \frac{\bar{v}T_4}{2L_1M_1} \left(\frac{T_2}{T_4} - \frac{T_3}{T_4} \right) + \frac{\bar{v}T_4}{2L_1M_2} (r-1) \right]}. \quad (44)$$

According to [71], the dimensionless efficient power of the QRHE cycle is defined as

$$\bar{W}_{ep} = W_{ep}/(W_{ep})_{\max}. \quad (45)$$

The occupancy probability of the first excited state of the system in each state i ($i = 1, 2, 3, 4$) is given by Gibbs distribution [9, 72]

$$p_{12} = 1/\left[1 + \exp(\Delta_1/(k_B T_1))\right], \quad (46)$$

$$p_{22} = 1/\left[1 + \exp(\Delta_2/(k_B T_2))\right], \quad (47)$$

$$p_{32} = 1/\left[1 + \exp(\Delta_3/(k_B T_3))\right], \quad (48)$$

$$p_{42} = 1/\left[1 + \exp(\Delta_4/(k_B T_4))\right], \quad (49)$$

where $\Delta_i = E_{i2} - E_{i1}$ is the energy level width of each state i ($i = 1, 2, 3, 4$), and k_B is Boltzmann constant.

From (4), one can obtain

$$\Delta_1 = \Delta_4 = \frac{3\pi^2\hbar^2}{2mL_1^2}, \quad (50)$$

$$\Delta_2 = \Delta_3 = \frac{3\pi^2\hbar^2}{2mL_2^2}. \quad (51)$$

From (13), one can obtain

$$p_{22} = [x^3(1+3p_{12})-1]/3. \quad (52)$$

From (24), one can obtain

$$p_{32} = [x^3(1+3p_{42})-1]/3. \quad (53)$$

From (46), (49), and (50), one can obtain

$$p_{42} = 1/\left[1 + \exp((\ln(1/p_{12}-1))r)\right]. \quad (54)$$

5. Single-objective performance analysis and optimization of QRHE cycle

Take $\xi_1 = \frac{\bar{v}T_4}{2L_1M_1} = 0.08$ and $\xi_2 = \frac{\bar{v}T_4}{2L_1M_2} = 0.06$ in the calculations, where ξ_1 and ξ_2 are dimensionless pure numbers determined by the system.

5.1. Dimensionless power and thermal efficiency

Figures 3–5 show the effects of cyclic parameters on \bar{P} and η characteristics. Figures 3 and 4 show the variation trends of \bar{P} and η with p_1 (occupation probabilities of the particles in the first excited state at state point 1) and x , respectively. In the

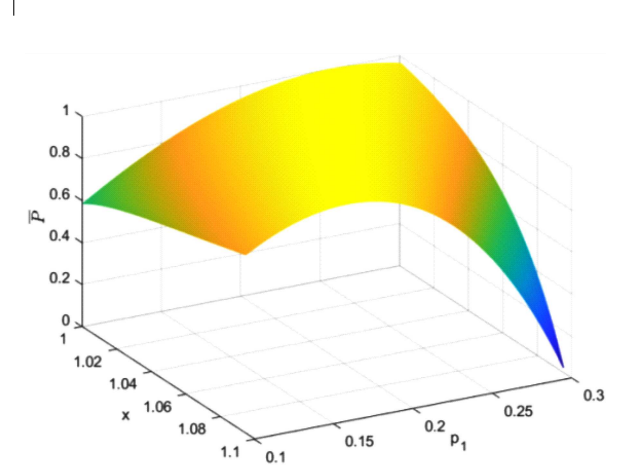


Fig. 3. Characteristics of \bar{P} versus x and p_1 .

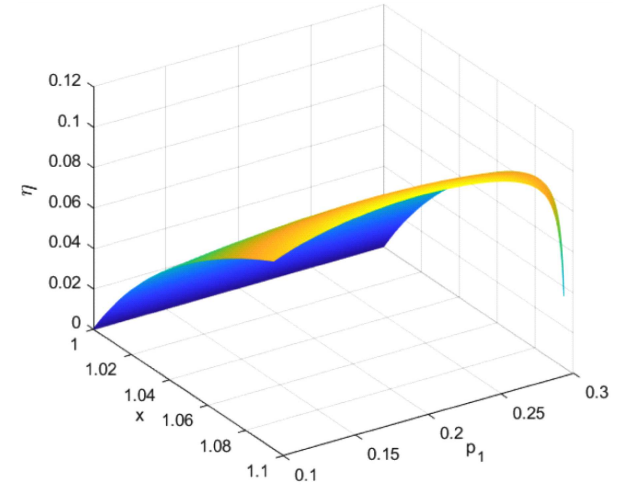


Fig. 4. Characteristics of η versus x and p_1 .

calculation, the temperature ratio $r = 2$ of WM and $\alpha = 0.1$ are taken. Figure 3 shows that the change trend of \bar{P} with $x(p_1)$ presents a convex and monotonous relationship, and there are \bar{P}_{\max} and a corresponding optimal $x_{m\bar{P}}(p_{1m\bar{P}})$. That is, $x_{m\bar{P}} = 1.093$ and $p_{1m\bar{P}} = 0.166$. Figure 4 shows that the change trend of η with $x(p_1)$ is also convex and monotonous, and there exists η_{\max} and a corresponding optimal $x_{m\eta}(p_{1m\eta})$. That is, $x_{m\eta} = 1.095$ and $p_{1m\eta} = 0.198$.

Figure 5 shows the influence of α on $\bar{P} - \eta$ performance. In the analysis, the potential well width ratio x is taken as the control variable, and p_1 is taken

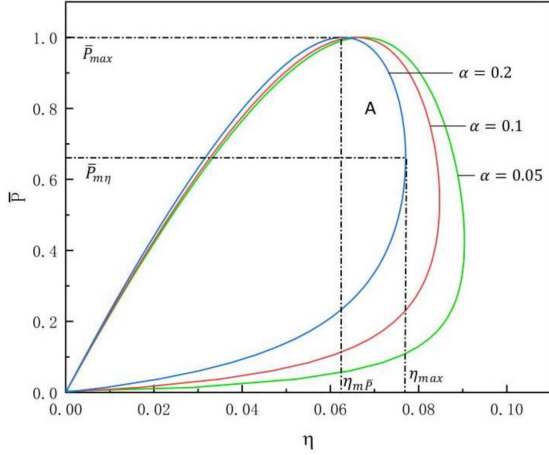


Fig. 5. Characteristics of η versus \bar{P} with $p_1 = 0.3$ and x as the control variable.

as the fixed value $p_1 = 0.3$. The result shows that the relationship curve is a loop-shaped curve. Take $\alpha = 0.2$ as an example, there is \bar{P}_{max} and corresponding $\eta_{m\bar{P}}$ in the curve. There are also η_{max} and corresponding $\bar{P}_{m\eta}$. The section (named section A) between point $(\eta_{m\bar{P}}, \bar{P}_{max})$ and point $(\eta_{max}, \bar{P}_{m\eta})$ is the optimal design range of the QRHE cycle. In this range, higher power can be obtained by sacrificing part of the efficiency, and higher efficiency can be obtained by reducing part of the power. It can be seen in the figure that α has an impact on the relationship curve of $\bar{P}(\eta)$. With the increase in α , $\eta_{m\bar{P}}$ and η_{max} decrease. Numerical computations show that as α is increased from 0.05 to 0.2, $\eta_{m\bar{P}}$ decreases from 0.0674 to 0.0629 (i.e., by about 6.68%), and η_{max} decreases from 0.0904 to 0.0771 (i.e., by about 14.71%). The outcomes show that as α increases, the optimal design range shrinks.

5.2. Dimensionless efficient power

Figures 6–9 show the influences of cycle parameters on \bar{W}_{ep} . Figures 6 and 7 show the effects of α and r on the performance of $(\bar{W}_{ep} - x)$, respectively. The two relationship curves shown in the figures are both parabolic-like. Since \bar{W}_{ep} first increases and then decreases as a function of x , there exists an optimal x to maximize efficient power. One can see that $x_{m\bar{W}_{ep}}$ corresponding to \bar{W}_{epmax} changes with the changes in α and r . With the increase in α , $x_{m\bar{W}_{ep}}$ decreases. As r increases, so does $x_{m\bar{W}_{ep}}$. Numerical computations show that as α is increased from 0.05 to 0.2, $x_{m\bar{W}_{ep}}$ decreases from 1.0610 to 1.0600 (i.e., by about 0.094%). When r increases from 1.5 to 2.5, $x_{m\bar{W}_{ep}}$ increases from 1.0565 to 1.0625 (i.e., by about 0.56%). Figure 8 shows the influence of α on $\bar{W}_{ep} - \eta$ performance. As can be seen, the relationship curve is a loop-shaped curve returning to the origin; \bar{W}_{epmax} and its corresponding $\eta_{m\bar{W}_{ep}}$ exist, and so do η_{max} and its corresponding $\bar{W}_{epm\eta}$.

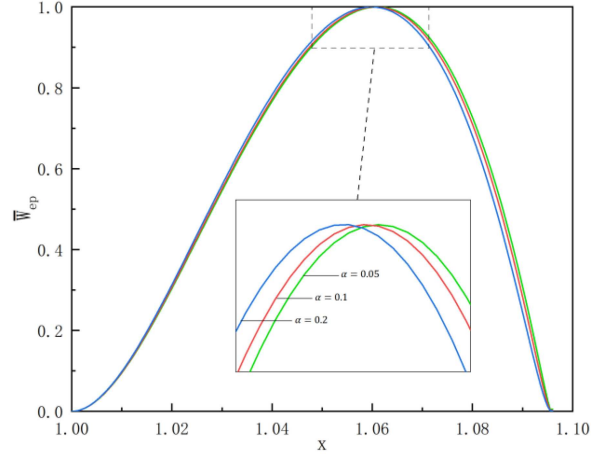


Fig. 6. Effect of α on cycle $\bar{W}_{ep} - x$.

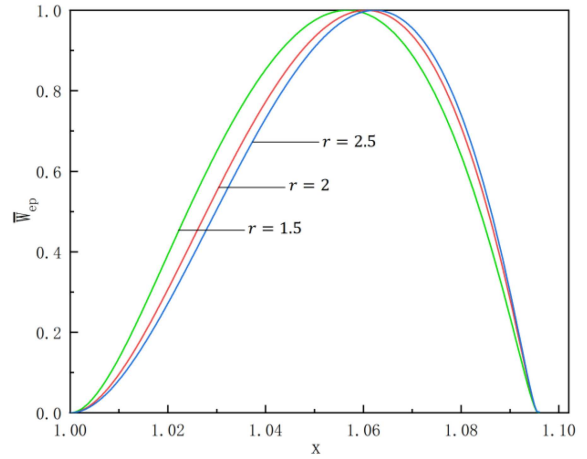


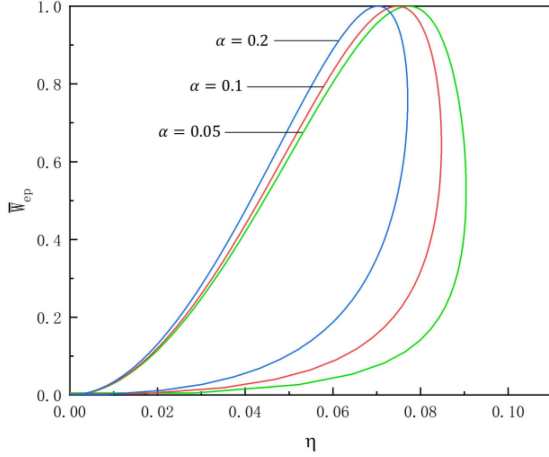
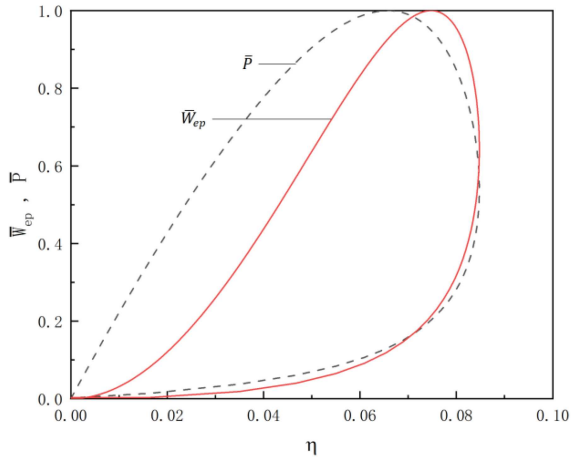
Fig. 7. Effect of r on cycle $\bar{W}_{ep} - x$.

With the increase in α , $\eta_{m\bar{W}_{ep}}$ decreases. When α increases from 0.05 to 0.2, $\eta_{m\bar{W}_{ep}}$ decreases from 0.07724 to 0.07042 (i.e., by about 8.83%).

Figure 9 shows the relationship curves of $\bar{W}_{ep} - \eta$ and $\bar{P} - \eta$ when $\alpha = 0.1$ is satisfied. One can see that $\eta_{m\bar{W}_{ep}}$ is greater than $\eta_{m\bar{P}}$. Numerical computations show that when \bar{W}_{epmax} is taken, the corresponding \bar{P} is 0.95032, the corresponding η is 0.07469, and η corresponding to \bar{P}_{max} is 0.06584. Compared with \bar{W}_{epmax} , the value of \bar{P} corresponding to \bar{W}_{epmax} is reduced by 4.968%. However, the η value corresponding to \bar{W}_{epmax} is about 13.442% higher than that of \bar{W}_{epmax} . The outcomes show that the efficient power considers both efficiency and power performance.

6. Multi-objective optimization of QRHE cycle

On the premise of multiple objective functions, it is often impossible to balance relationships among various objective functions by using univariate


 Fig. 8. Effect of α on cycle $\bar{W}_{ep} - \eta$.

 Fig. 9. Characteristics of $\bar{W}_{ep} - \eta$ and $\bar{P} - \eta$ when $\alpha = 0.1$.

optimization. The multi-objective optimization algorithm can weigh the advantages and disadvantages of each objective function so as to achieve the best compromise of different objective functions. A series of non-inferior solutions are obtained, which are called the Pareto frontier. According to the processing method of [48–58, 73, 74], this paper uses the NSGA-II algorithm, which is widely used to solve the problem of multi-objective optimization.

This paper takes x as the optimization variable and takes η , \bar{P} , and \bar{W}_{ep} as objective functions for MOO. Three decision-making methods, namely LINMAP, TOPSIS, and Shannon entropy, are adopted to optimize the cycle with either two or three objectives and obtain a series of Pareto frontiers under various combinations.

Any combination of two objective functions can give three two-objective optimization expressions

$$\max \left\{ \begin{array}{l} \bar{P}(x) \\ \eta(x) \end{array} \right\}, \quad \max \left\{ \begin{array}{l} \bar{P}(x) \\ \bar{W}_{ep}(x) \end{array} \right\}, \quad \max \left\{ \begin{array}{l} \eta(x) \\ \bar{W}_{ep}(x) \end{array} \right\}. \quad (55)$$

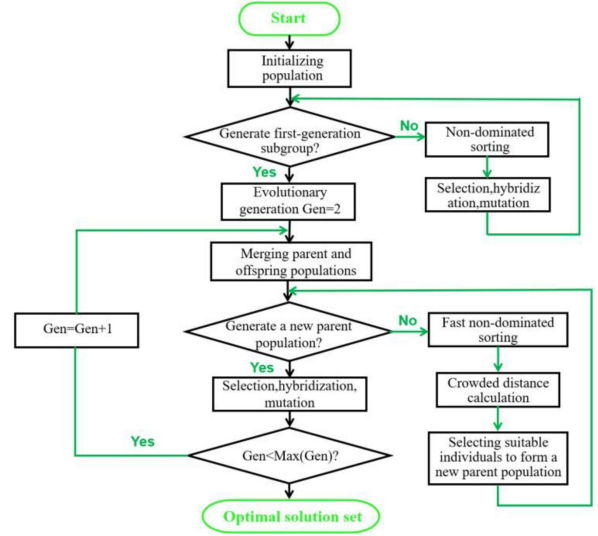


Fig. 10. Algorithm flow chart of NSGA-II.

Any combination of three objective functions can give a three-objective optimization expression

$$\max \left\{ \begin{array}{l} \bar{P}(x) \\ \eta(x) \\ \bar{W}_{ep}(x) \end{array} \right\}. \quad (56)$$

The deviation index D represents the ideal degree of the results under the optimization scheme, and the smaller the value, the better. The better design scheme is determined by the smaller deviation index D . Figure 10 is the algorithm flow chart of NSGA-II.

Table I lists the outcomes of single-, double-, and triple-objective optimizations for the QRHE cycle. For triple-objective optimization combination $(\bar{P}, \eta, \bar{W}_{ep})$, it is one group. The deviation index D s obtained using TOPSIS, LINMAP, and Shannon entropy decision-making are the same, i.e., 0.0737. The combination of the double-objective optimizations includes three groups, and the deviation index D obtained by Shannon entropy decision-making for the combination of η and \bar{W}_{ep} is the smallest, i.e., 0.0269. However, for the single-objective optimizations with maximum η , \bar{P} , and \bar{W}_{ep} , the deviation index D s are 0.9752, 0.0806, and 0.0890, respectively. The outcomes show that a more ideal design scheme can be obtained by using MOO.

Figures 11–13 show the Pareto frontier diagram of three combinations of double-objective optimizations. Note that η and \bar{W}_{ep} decrease with increasing \bar{P} , and \bar{W}_{ep} decreases with increasing η . Table I displays that the deviation index D is smaller when using the TOPSIS decision-making approach to optimize \bar{P} and η or \bar{P} and \bar{W}_{ep} . When using the Shannon Entropy decision-making approach to optimize η and \bar{W}_{ep} , the deviation index D is smaller. Figure 14 shows mean distance and mean

Optimization results with single-objective, double-objective, and triple-objective.

TABLE I

Objective combination	Decision-making approach	Optimization variable	Objective function			Deviation index
		x	\bar{P}	η	\bar{W}_{ep}	D
Triple-objective optimization (\bar{P} , η , and \bar{W}_{ep})	LINMAP	1.0610	0.9455	0.0773	1.0000	0.0737
	TOPSIS	1.0610	0.9455	0.0773	1.0000	0.0737
	Shannon entropy	1.0610	0.9455	0.0773	1.0000	0.0737
Double-objective optimization (\bar{P} and η)	LINMAP	1.0623	0.9325	0.0782	0.9989	0.1190
	TOPSIS	1.0609	0.9466	0.0772	1.0000	0.0953
	Shannon entropy	1.0855	0.4243	0.0904	0.5250	0.9615
Double-objective optimization (\bar{P} and \bar{W}_{ep})	LINMAP	1.0560	0.9826	0.0732	0.9846	0.2421
	TOPSIS	1.0563	0.9813	0.0734	0.9860	0.2415
	Shannon entropy	1.0610	0.9455	0.0773	1.0000	0.4107
Double-objective optimization (η and \bar{W}_{ep})	LINMAP	1.0687	0.8459	0.0828	0.9593	0.0870
	TOPSIS	1.0679	0.8593	0.0823	0.9679	0.0695
	Shannon entropy	1.0610	0.9455	0.0773	1.0000	0.0269
maximum \bar{P}		1.0495	1.0000	0.0674	0.9232	0.0806
maximum η		1.0855	0.4234	0.0904	0.5240	0.9752
maximum \bar{W}_{ep}		1.0610	0.9457	0.0772	1.0000	0.0890
positive ideal point		—	1.0000	0.0904	1.0000	—
negative ideal point		—	0.4243	0.0673	0.5250	—

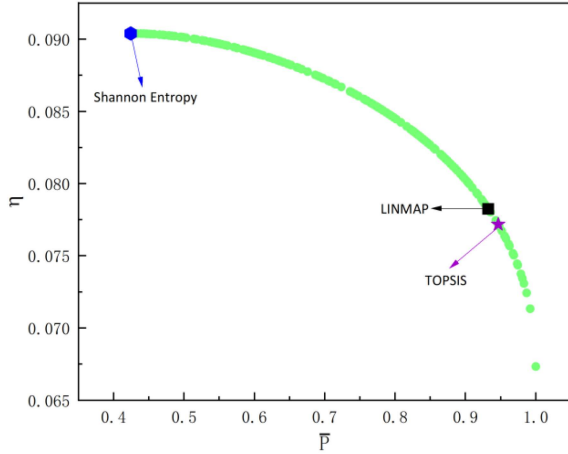


Fig. 11. Pareto frontier of double-objective optimization with $\bar{P} - \eta$ combination.

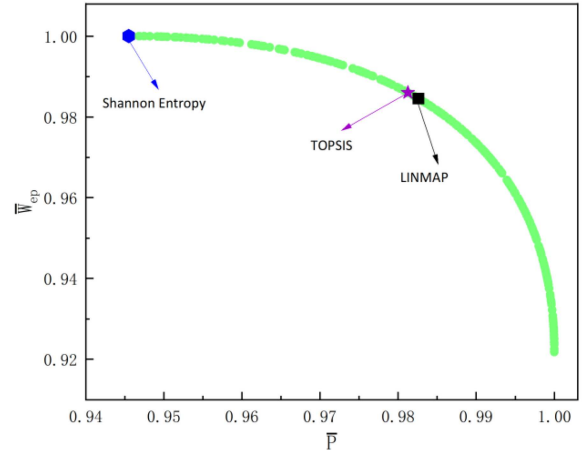


Fig. 12. Pareto frontier of double-objective optimization with $\bar{P} - \bar{W}_{ep}$ combination.

distribution vs. number of generations of genetic algorithm when taking η and \bar{W}_{ep} as optimization objectives. The algorithm converges in the 716th generation.

Figure 15 shows the Pareto frontier diagram of triple-objective optimization. When \bar{P} increases, η decreases, and \bar{W}_{ep} increases initially and then decreases. The point at which \bar{P} , η , and \bar{W}_{ep} all reach their maximum is called a positive ideal point, and the point at which both reach their minimum is called a negative ideal point. Neither the positive nor negative ideal points lie on the Pareto front.

Table I shows that the deviation index D_s obtained when optimizing \bar{P} , η , and \bar{W}_{ep} by using

TOPSIS, LINMAP, and Shannon entropy decision-making approaches are consistent. Figure 16 shows mean distance and mean distribution vs. number of generations of genetic algorithm when \bar{P} , η , and \bar{W}_{ep} are the optimization objectives. In the 805th generation, the genetic algorithm converges.

7. Conclusions

In this paper, a QRHE cycle model with countless particles trapped in OIPW as WM is established considering heat leakage. By using FTT and quantum thermodynamics, expressions of η , \bar{P} , and \bar{W}_{ep}

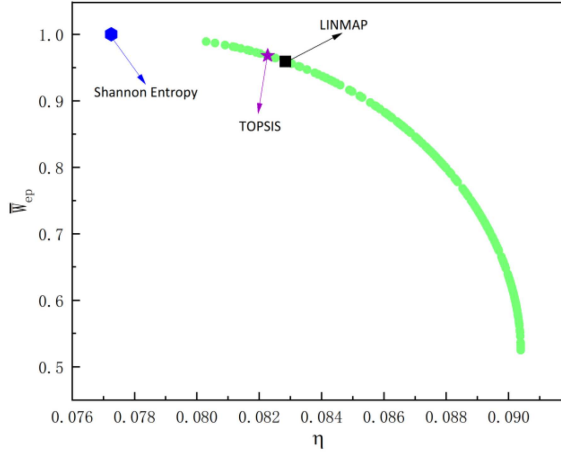


Fig. 13. Pareto frontier of double-objective optimization with $\eta - \bar{W}_{ep}$ combination.

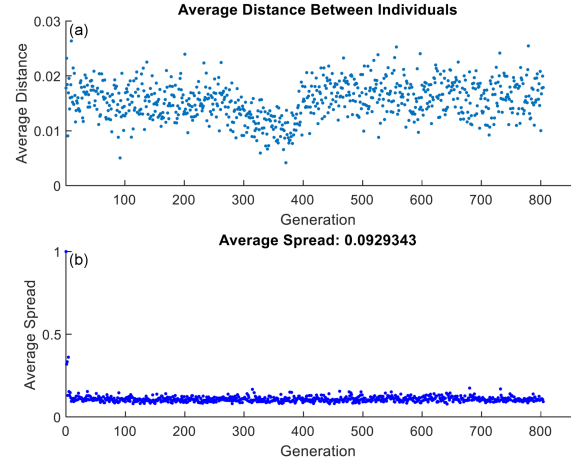


Fig. 16. Mean distance and mean spread versus number of generations of triple-objective optimization with $\bar{P} - \eta - \bar{W}_{ep}$ combination.

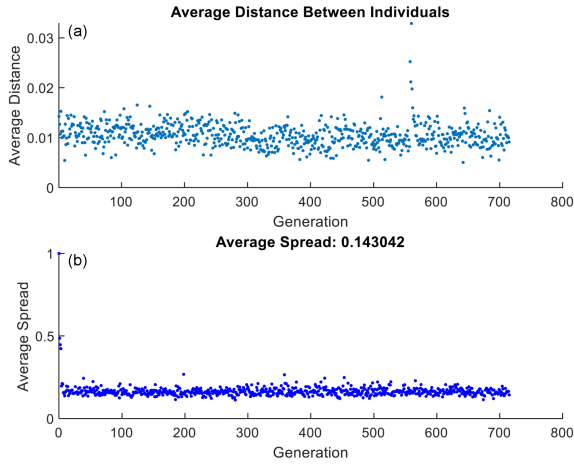


Fig. 14. Mean distance and mean spread versus number of generations of double-objective optimization with $\eta - \bar{W}_{ep}$ combination.

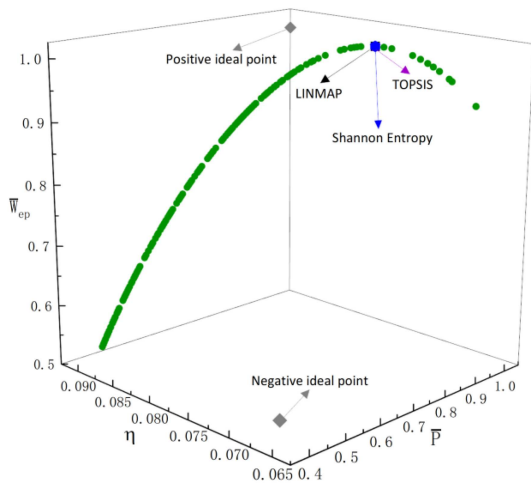


Fig. 15. Pareto frontier of triple-objective optimization with $\bar{P} - \eta - \bar{W}_{ep}$ combination.

of the QRHE cycle are derived, and the optimal performances of the QRHE cycle are investigated. Intermediate variable x is taken as the optimization variable. Utilizing the NSGA-II algorithm, \bar{P} , η , and \bar{W}_{ep} are taken as the objective functions to carry out MOO. Pareto frontiers of different objective function combinations are obtained. TOPSIS, LINMAP, and Shannon entropy decision-making approaches are adopted to select the optimal design with deviation index D as the evaluation indicator. The outcomes display that:

1. Both the relationships between \bar{P} and $x(p_1)$ as well as between η and $x(p_1)$ are convex and monotonous. If x is the control variable, the relationship curve between \bar{P} and η is a loop-shaped curve. The optimal design range of the QRHE cycle lies between \bar{P}_{\max} and η_{\max} . As α increases, the optimal QRHE cycle design range shrinks.
2. The relationship curve $\bar{W}_{ep} - x$ is parabolic-like, and there exists an optimal $x_{m\bar{W}_{ep}}$ to maximize efficient power. With increasing α and decreasing r , $x_{m\bar{W}_{ep}}$ decreases. The relationship $\bar{W}_{ep} - \eta$ is a loop-shaped curve returning to the origin. As α increases, the value of $\eta_{m\bar{W}_{ep}}$ at $\bar{W}_{ep\max}$ decreases. Compared with \bar{P}_{\max} , when efficient power is taken as the optimization target, the optimization outcomes take into account both the larger power and the higher efficiency. At this time, the QRHE cycle sacrifices part of the power in exchange for an increase in efficiency.
3. When MOO is carried out with η and \bar{W}_{ep} as optimization objectives, the smallest deviation index D inferred by Shannon entropy decision-making is 0.0269. Its design scheme is closest to the ideal scheme. In order to optimize the objective of other

combinations, an appropriate decision-making scheme should be chosen based on actual requirements.

The outcomes of this paper have some theoretical reference meanings for the design of the QRHE cycle with countless particles trapped in OIPW and with heat leakage. Meanwhile, one may find some new characteristics in quantum rectangular cycles by studying them. These characteristics may include cycle structure, cycle control strategy, energy transfer and transmission mechanism, and so on. This is worthy of further study and exploration.^{†1}

Acknowledgments

This paper is supported by the National Natural Science Foundation of China (Project Nos. 52171317 and 51779262). The authors wish to thank the reviewers for their careful, unbiased, and constructive suggestions, which led to this revised manuscript.

References

- [1] H. Terças, S. Ribeiro, M. Pezzutto, Y. Omar, *Phys. Rev. E* **95**, 022135 (2017).
- [2] R. Kosloff, *J. Chem. Phys.* **150**, 204105 (2019).
- [3] S. Singh, *Int. J. Theor. Phys.* **59**, 2889 (2020).
- [4] R. Dann, R. Kosloff, *New J. Phys.* **25**, 043019 (2023).
- [5] A. Fahriza, T.E.P. Sutantyo, Z. Abdullah, *Eur. Phys. J. Plus* **137**, 1030 (2022).
- [6] N.M. Myers, O. Abah, S. Deffner, *AVS Quantum Sci.* **4**, 027101 (2022).
- [7] H.E.D. Scovil, E.O. Schulz-DuBois, *Phys. Rev. Lett.* **2**, 262 (1959).
- [8] Y. Yin, F. Wu, L.G. Chen, *J. Eng. Thermophys.* **38**, 2061 (2017).
- [9] Y. Yin, L.G. Chen, Wu, F. *Phys. A* **503**, 58 (2018).
- [10] X.W. Liu, L.G. Chen, Y.L. Ge, J.H. Feng, F. Wu, *J. Non-Equil. Thermodyn.* **46**, 61 (2021).
- [11] L.G. Chen, X.W. Liu, F. Wu, H.J. Feng, S.J. Xia, *Phys. A* **550**, 124140 (2020).
- [12] L.G. Chen, Z.W. Meng, Y.L. Ge, F. Wu, *Entropy* **23**, 536 (2021).
- [13] B. Andresen, *Finite-Time Thermodynamics*, University of Copenhagen, Copenhagen (Denmark) 1983.
- [14] L.G. Chen, C. Wu, F.R. Sun, *J. Non-Equilib. Thermodyn.* **24**, 327 (1999).
- [15] R.S. Berry, P. Salamon, B. Andresen, *Entropy* **22**, 908 (2020).
- [16] S.S. Qiu, Z.M. Ding, L.G. Chen, Y.L. Ge, *Sci. China Technol. Sci.* **64**, 1007 (2021).
- [17] S.S. Qiu, Z.M. Ding, L.G. Chen, Y.L. Ge, *Sci. China Technol. Sci.* **64**, 1641 (2021).
- [18] Z.M. Ding, S.S. Qiu, L.G. Chen, W.H. Wang, *J. Non-Equilib. Thermodyn.* **46**, 273 (2021).
- [19] Y. Bassie, T. Birhanu, Y. Abebe, A. Abawari, [arXiv:2207.00867v1](https://arxiv.org/abs/2207.00867v1), 2022.
- [20] L.G. Chen, S.J. Xia, *J. Non-Equilib. Thermodyn.* **47**, 329 (2022).
- [21] J. Li, L.G. Chen, *J. Non-Equilib. Thermodyn.* **47**, 433 (2022).
- [22] L.G. Chen, S.J. Xia, *Sci. China Technol. Sci.* **66**, 841 (2023).
- [23] L.G. Chen, S.J. Xia, *Sci. China Technol. Sci.* **66**, 2651 (2023).
- [24] L.G. Chen, Xia, S.J. *J. Non-Equilib. Thermodyn.* **48**, 41 (2023).
- [25] L.G. Chen, S.J. Xia, *J. Non-Equilib. Thermodyn.* **48**, 107 (2023).
- [26] L.G. Chen, S.S. Shi, H.J. Feng, Y.L. Ge, *J. Non-Equilib. Thermodyn.* **48**, 179 (2023).
- [27] D. Wu, Y.L. Ge, L.G. Chen, L. Tian, *J. Non-Equilib. Thermodyn.* **48**, 477 (2023).
- [28] L.G. Chen, X.W. Liu, F. Wu, S.J. Xia, H.J. Feng, *Phys. A* **537**, 122597 (2020).
- [29] S. Singh, S. Rebari, *Eur. Phys. J. B* **93**, 150 (2020).
- [30] X.L. Huang, L.C. Wang, X.X. Yi, *Phys. Rev. E* **87**, 012144 (2013).
- [31] X.W. Liu, L.G. Chen, S.H. Wei, F.K. Meng, *J. Thermal Sci. Eng. Appl.* **12**, 011007 (2020).
- [32] R. Kosloff, Rezek, Y. *Entropy* **19**, 136 (2017).
- [33] S. Chand, S. Dasgupta, A. Biswas, *Phys. Rev. E* **103**, 032144 (2021).
- [34] R. Kosloff, *J. Chem. Phys.* **80**, 1625 (1984).
- [35] M.O. Scully, K.R. Chapin, K.E. Dorfman, A. Svidzinsky, *Proc. Natl. Acad. Sci.* **108**, 15097 (2011).
- [36] R.S. Whitney, *Phys. Rev. Lett.* **112**, 130601 (2014).
- [37] A.Q. Shu, F. Wu, *Acta Phys. Sin.* **65**, 044304 (2016).

^{†1}The datasets generated and/or analyzed during the current study are available from the corresponding author upon reasonable request.

- [38] Z.J. Yan, *P. Chin. J. Nat.* **7**, 475 (1984).
- [39] T. Yilmaz, *J. Energy Instit.* **79**, 38 (2006).
- [40] H.T. Quan, Y. Liu, C.P. Sun, F. Nori, *Phys. Rev. E* **76**, 031105 (2007).
- [41] V. Singh, *Phys. Rev. Res.* **2**, 043187 (2020).
- [42] K. Kaur, A. Jain, L.S. Singh, R. Singla, S. Rebari, [arXiv:2301.03927v1](https://arxiv.org/abs/2301.03927v1), 2023.
- [43] M.F. da Silva Ferreira, *Eur. J. Phys.* **33**, 13 (2012).
- [44] X. Liu, L.G. Chen, X.Y. Qin, Y.L. Ge, F.R. Sun, *Energy Conserv.* **32**, 19 (2013).
- [45] C. Wang, L.G. Chen, Y.L. Ge, F.R. Sun, *Int. J. Energy Environ.* **6**, 73 (2015).
- [46] C. Wang, L.G. Chen, Y.L. Ge, F.R. Sun, *Appl. Thermal Eng.* **109**, 507 (2016).
- [47] M.H. Ahmadi, H. Hosseinzade, H. Sayyaadi, A.H. Mohammadi, F. Kimiaghali, *Renew Energy* **60**, 313 (2013).
- [48] Q.R. Gong, Y.L. Ge, L.G. Chen, S.S. Shi, J.H. Feng, *Entropy* **23**, 1203 (2021).
- [49] X.H. Liu, Q.R. Gong, L.G. Chen, Y.L. Ge, *Energy Rep.* **8**, 12712 (2022).
- [50] X.F. Qiu, L.G. Chen, Y.L. Ge, Q.R. Gong, J.H. Feng, *Case Stud. Therm. Eng.* **39**, 102415 (2022).
- [51] X.F. Qiu, L.G. Chen, Y.L. Ge, S.S. Shi, *Entropy* **24**, 1531 (2022).
- [52] Y.L. Ge, S.S. Shi, L.G. Chen, D.F. Zhang, H.J. Feng, *J. Non-Equilib. Thermodyn.* **47**, 289 (2022).
- [53] H.R. Xu, L.G. Chen, Y.L. Ge, H.J. Feng, *Energy* **256**, 124699 (2022).
- [54] P.C. Zang, Y.L. Ge, L.G. Chen, Q.R. Gong, *Case Stud. Therm. Eng.* **35**, 102154 (2022).
- [55] W.H. Yang, H.J. Feng, L.G. Chen, Y.L. Ge, *Energy* **278**, 127755 (2023).
- [56] L.G. Chen, S.S. Shi, Y.L. Ge, H.J. Feng, *Energy* **282**, 128717 (2023).
- [57] L.G. Chen, S.S. Shi, Y.L. Ge, H.J. Feng, *Energy* **282**, 128817 (2023).
- [58] L.G. Chen, P.L. Li, S.J. Xia, R. Kong, Y.L. Ge, *Sci. China Technol. Sci.* **65**, 1396 (2022).
- [59] P.L. Li, L.G. Chen, S.J. Xia, R. Kong, Y.L. Ge, *Sci. China Technol. Sci.* **65**, 657 (2022).
- [60] P.A. Erdman, A. Rolandi, P. Abiuso, M. Perarnau-Llobet, F. Noe, *Phys. Rev. Research* **5**, L022017 (2023).
- [61] E. Açıkkalp, N. Caner, *Eur. Phys. J. Plus* **130**, 73 (2015).
- [62] Y.D. Saputra, *Positron* **9**, 81 (2019).
- [63] Y.D. Saputra, *J. Phys. Conf. Ser.* **1726**, 012016 (2021).
- [64] X.W. Liu, L.G. Chen, F. Wu, F.R. Sun, *Math. Comput. Modelling* **54**, 190 (2011).
- [65] F. Wu, L.G. Chen, F.R. Sun, C. Wu, Q. Li, *Phys. Rev. E* **73**, 016103 (2006).
- [66] F. Jain, S. Cheung, W. Huang, *Int. J. Infrared Millim. Waves* **21**, 759 (2000).
- [67] J.H. Wang, *Study on the Performance of Finite Time Thermodynamic Cycles*, Nanchang University, Nanchang (China) 2007.
- [68] J.W. Zhang, J.Q. Zhang, G.Y. Ding, J.C. Li, J.T. Bu, B. Wang, L.L. Yan, S.L. Su, L. Chen, F. Nori, Ş.K. Özdemir, F. Zhou, H. Jing, M. Feng, *Nat. Commun.* **13**, 6225 (2022).
- [69] X.F. Nie, X.R. Zhu, C. Xi, X.Y. Long, Z.D. Lin, Y. Tian, C.D. Qiu, X.D. Yang, Y. Dong, J. Li, T. Xin, D.W. Lu, *Phys. Rev. Lett.* **129**, 100603 (2022).
- [70] C.J. Ou, S. Abe, *Europhys. Lett.* **113**, 40009 (2016).
- [71] R. Kumar, S.C. Kaushik, R. Kumar, *Int. J. Eng. Res. Technol.* **6**, 643 (2013).
- [72] S.N. Liu, C.J. Ou, *Entropy* **18**, 205 (2016).
- [73] L. Tian, L.G. Chen, Y.L. Ge, S.S. Shi, *Entropy* **24**, 1443 (2022).
- [74] J.H. He, L.G. Chen, Y.L. Ge, S.S. Shi, F. Li, *Entropy* **24**, 1445 (2022).